

Finite-Element Modeling of Titanium Powder Densification

BING YE, MARC R. MATSEN, and DAVID C. DUNAND

A powder-level, finite-element model is created to describe densification, as a function of applied stress during uniaxial hot pressing, of CP-Ti and Ti-6Al-4V powders with spherical or spheroidal shapes for various packing geometries. Two cases are considered: (1) isothermal densification (in the α - or β -fields of CP-Ti and in the β -field of Ti-6Al-4V) where power-law creep dominates and (2) thermal cycling densification (across the α/β -phase transformation of Ti-6Al-4V) where transformation mismatch plasticity controls deformation at low stresses. Reasonable agreement is achieved between numerical results and previously published experimental measurements and continuum modeling predictions.

DOI: 10.1007/s11661-011-0839-0

© The Minerals, Metals & Materials Society and ASM International 2011

I. INTRODUCTION

HIGH-temperature powder compaction is a well-established method to create complex shapes with good mechanical properties from Ti-6Al-4V, which are the work-horse titanium alloys in the aerospace^[1,2] and biomedical industries.^[3–6] Powder densification at increased temperature is accelerated by the application of an external stress,^[7–10] through deformation at contact points between powders, which is controlled by the power-law creep mechanism with the constitutive equation

$$\dot{\varepsilon}_x = C \cdot \sigma_x^n \quad [1]$$

where $\dot{\varepsilon}_x$ is the steady-state (secondary) uniaxial strain rate, σ_x is the uniaxial stress, C is a constant incorporating an Arrhenius temperature dependence ($C = 4.8 \times 10^{-7} \text{ MPa}^{-2.8} \text{s}^{-1}$ for Ti-6Al-4V at 1293 K (1020 °C)^[11,12]), and n is the creep stress exponent ($n = 2.8$ for Ti-6Al-4V^[12]). Based on Eq. [1], equations predicting densification kinetics (density vs time) can then be derived^[7–9,13–16] for an assembly of spherical powders with initial relative density ρ_0 subjected to an external stress σ in a uniaxial die pressing experiment. The densification rates $\dot{\rho}$ for initial stage densification (relative density $\rho < 90$ pct, where deformation of powders at contact points and increasing coordination number are important) and final stage densification ($\rho > 90$ pct, considering the shrinkage of individual pores in a matrix) are respectively given as follows:

$$\dot{\rho}_I = 3.06 \cdot C \cdot \left(\frac{1 - \rho_0}{\rho - \rho_0} \right)^{n-1/2} \frac{\rho_0^{1/3}}{\rho^{2n-2/3}} \cdot \left(\frac{B_i \cdot \sigma}{3} \right)^n \quad [2]$$

BING YE, Postdoctoral Fellow, and DAVID C. DUNAND, Professor, are with the Department of Materials Science and Engineering, Northwestern University, Evanston, IL 60208. Contact e-mail: dunand@northwestern.edu MARC R. MATSEN, Boeing Technical Fellow, is with Boeing Research and Technology, The Boeing Company, Seattle, WA 98124.

Manuscript submitted January 25, 2011.

Article published online August 3, 2011

$$\dot{\rho}_{II} = \frac{3}{2} \cdot C \cdot \frac{\rho \cdot (1 - \rho)}{(1 - (1 - \rho)^{1/n})^n} \cdot \left(\frac{3B_f \cdot \sigma}{2 \cdot n} \right)^n \quad [3]$$

where ρ_0 is the initial powder density and the constants B_i and B_f take into account compaction geometry ($B_i = 1.1$ and $B_f = 1.8$ for uniaxial die pressing^[15]). When thermally cycled between its allotropic α - and β -phases, Ti-6Al-4V exhibits transformation mismatch plasticity^[11,12,17–20] with a constitutive equation given by

$$\bar{\dot{\varepsilon}}_x = \frac{4}{3} \cdot \frac{5 \cdot n}{4 \cdot n + 1} \cdot \frac{\Delta V}{V} \cdot \frac{1}{\Delta t} \cdot \frac{\sigma_x}{\sigma_0} \quad [4]$$

where $\bar{\dot{\varepsilon}}_x$ is the average uniaxial strain rate during thermal-cycling transformation-mismatch plasticity; $\Delta V/V (=0.96$ pct) is the volume mismatch between the allotropic α and β phases^[11]; Δt is the period of the thermal cycles spanning two transformations on heating and cooling, respectively; and σ_0 is the average internal stress generated during the phase transformation ($\sigma_0 = 7.4$ MPa for Ti-6Al-4V^[11]). Transformation mismatch plasticity (Eq. [4]) is a special case of a creep-type equation (Eq. [1]) with creep stress exponent $n = 1$ and the other parameters in Eq. [4] merged as a constant C , with a value of $1.045 \times 10^{-5} \text{ MPa}^{-1} \text{s}^{-1}$ ^[11,16] for Ti-6Al-4V for thermal cycling 1133 K to 1293 K (860 °C to 1020 °C) with a period $\Delta t = 191$ seconds (with a heating time of 96 seconds and cooling time of 95 seconds under constant heating power during the thermal cycling experiment). The preceding creep-based powder densification models (Eqs. [2] and [3]) can then be applied to the case where transformation mismatch plasticity is active, as shown for densification of commercial purity titanium (CP-Ti)^[15] and Ti-6Al-4V.^[16]

An alternative modeling approach for modeling powder densification is based on the finite-element (FE) method. For powder densification modeling, some researchers have focused on developing macroscopic constitutive law^[21–30] without addressing explicitly the stress state within individual powders to minimize computation expenses. In this context, a discrete

element method (DEM)^[31] with a simplified interparticle contact model and explicit integration, has been developed to simulate macroscopic granular compactions, with thousands of powder particles. Because of limitation in the contact model, this approach is limited to the simulation of low relative densities processes such as cold compaction.^[32] With the growth of computational power and the desire to understand large particle permanent deformation and complex powder interaction during high-density powder compaction, powder-level (with multiple powder particles) FE simulations are becoming feasible and have been performed in two-dimensional^[33,34] and three-dimensional (3-D)^[35,36] for the case of cold compaction. The main difficulty is from the complexity of interpowder contact simulation. Furthermore, other approaches such as multi-scale framework,^[37] combination of DEM and FE methods^[38–41] with effective contact detection algorithm,^[42] and statistical modeling^[43] based on fine features from powder-level FE results^[33,38] are being actively developed. However, all the powder-level simulations conducted to date are confined to the elastic-plastic case during cold compaction, and we are not aware of simulations for the more complex case of power-law based creep densification at high temperature, relevant to hot pressing.

In the current article, we examine the densification of Ti-6Al-4V powders in a powder-level FE simulation, where powders deform by isothermal, creep conditions or under thermal cycling, transformation-mismatch plasticity conditions. We compute densification curves for various applied stresses for hot die pressing and compare these results to previous experimental data and predictions from continuum models (Eqs. [2] and [3]).^[8,15] We also examine the effects of powder shape

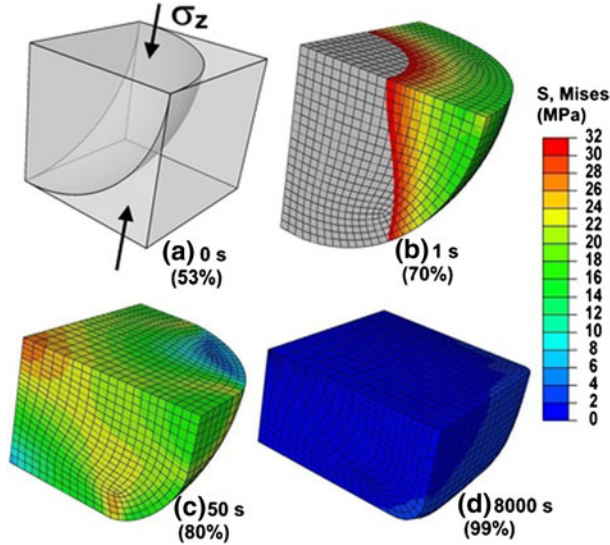


Fig. 1—FE densification simulation for simple cubic configuration (sc): (a) initial powder with 53 pct relative density and (b–d) von Mises stress contour plot of deformed powder at different time for Ti-6Al-4V at 15 MPa applied stress and 1293 K (1020 °C). The gray region represents stress greater than the maximum value in the color scale. Densification times and relative density are given under each figure.

and initial packing geometry on the stress distribution in the powders during densification and the resulting densification kinetics.

II. FINITE-ELEMENT MODEL

A. Simulation Approach

The FE simulation is complicated by the contacts between particles (necessitating contact penetration detection) and by the large strains accumulated. The computation was conducted on an eight CPU desktop computer using the parallel function of the commercial software suite ABAQUS/Standard 6.7-3 software of Dassault Systèmes (Lowell, MA) (improving accuracy as compared with ABAQUS/Explicit). During the simulation, the powders were in point contact in the initial configuration, corresponding to the configuration present after manually tapping the powders in a physical experiment. In such powder compaction experiments,

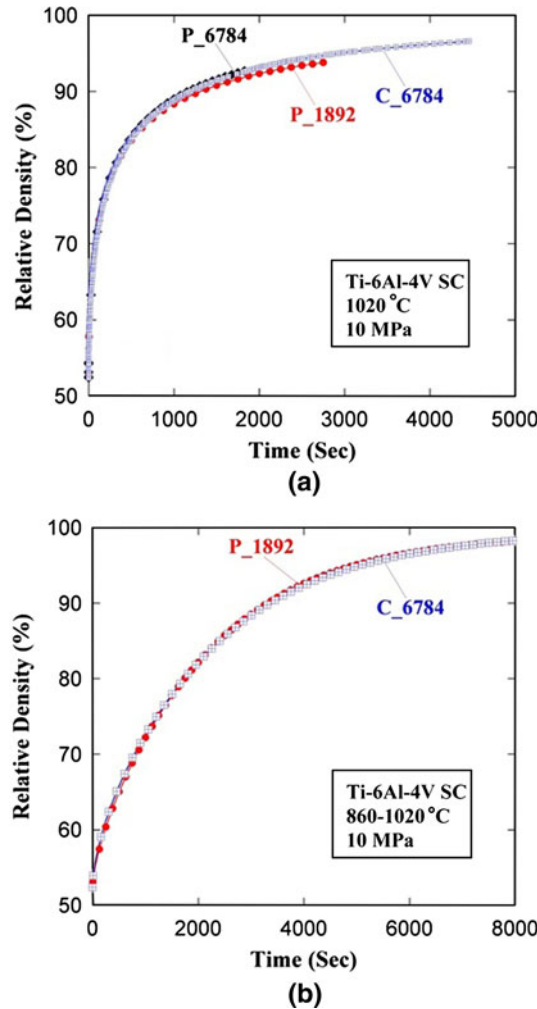


Fig. 2—FE densification curves for sc configuration for Ti-6Al-4V powders under 10 MPa stress deforming by (a) creep at 1293 K (1020 °C) and (b) transformation-plasticity 1133 K to 1293 K (860 °C to 1020 °C). Letters refer to model (P: plasticity, C: creep) and numbers to the number of elements.

the external stress is first gradually applied to the desired level and then kept constant until the end of the compaction. To translate the experiment to simulation and for better numerical stability, the simulation was divided into two stages: (1) the stress is ramped linearly over one second from zero to the final stress level and (2) the stress is maintained constant while densification takes place. Special care was used for modeling contact between powders. Initially, the tolerance for adjustment zone is zero for the contact adjustment between the slave node and surface. In stage (1) of the simulation, the contact was assured by an interference fit option named “gradually remove slave node over-closure by automatic shrink fit” in ABAQUS/Standard. In stage (2), the uniform allowable interference is by amplitude with a typical initial value of 0.0001 in ABAQUS/Standard, which is equivalent to 0.0001 μm for the real powders.

Because the densification is by creep deformation of the powders (Eq. [1]), the first intuitive choice for the ABAQUS simulation procedure is isotropic creep (using von Mises stress potential) under the “visco” procedure, where time can be tracked. In this procedure, creep integration is by a mixed explicit and implicit scheme for both accuracy and speed. The error was controlled by creep strain error tolerance parameter (CTEOL) ($\Delta\varepsilon$),

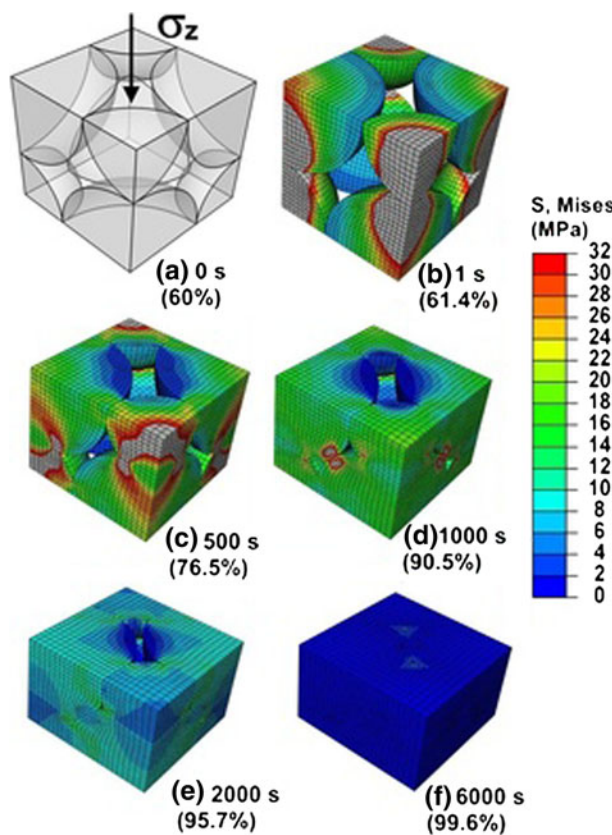


Fig. 3—FE densification simulation for simple cubic configuration with two different powder sizes (sc-2): (a) initial powder with relative density 60 pct, and (b-f) von Mises stress contour plot of deformed powder at different time for Ti-6Al-4V at 15 MPa applied stress and 1293 K (1020 °C). The gray region represents stress greater than maximum stress in the color scale. The densification times and relative density are given under each figure.

the ratio of force measurement error ($\Delta\sigma$) to the Young's modulus E, and a value of 2.3×10^{-6} was taken so that the force measurement error was about 0.1 MPa, or 1 pct for 10 MPa loading. The time-hardening (constant stress condition) and strain-hardening (stress varying condition) creep law in ABAQUS was limited in the applications where the stresses were relatively low. However, the contact front between powders had a high effective stress, so large permanent plastic deformation occurred there. With the specified error level by CTEOL, the simulation with creep by the “visco” procedure was rather slow for a single powder simulation. In the case of multiple powder simulation, e.g., face-centered cubic (fcc) configuration (as described in more details below), solution convergence was difficult without using a damping factor. With a damping factor, an unreasonable stable condition was often reached, which was indicated by the ratio of the viscous damping energy (called ALLSD in ABAQUS) or dissipated stabilization energy to the total strain energy (called ALLSE in ABAQUS) exceeding a reasonable fraction, which was below 5 pct for powder compaction without much rigid motion (as per ABAQUS Analysis User's Manual, Section 7.1.1). The problem of the damping effect was also indicated by the fast relaxation of von Mises stress, which led to a negligible strain rate (Eq. [1]) or densification rate. Fine tuning (including parameter study and parameter optimization for both accuracy and speed) was needed to use the creep procedure.

To improve computational efficiency, the creep simulations were carried out in ABAQUS with rate-dependent plasticity; Eq. [1] was rewritten as follows:

$$\sigma_x = (\dot{\varepsilon}_x/C)^{1/n} \quad [5]$$

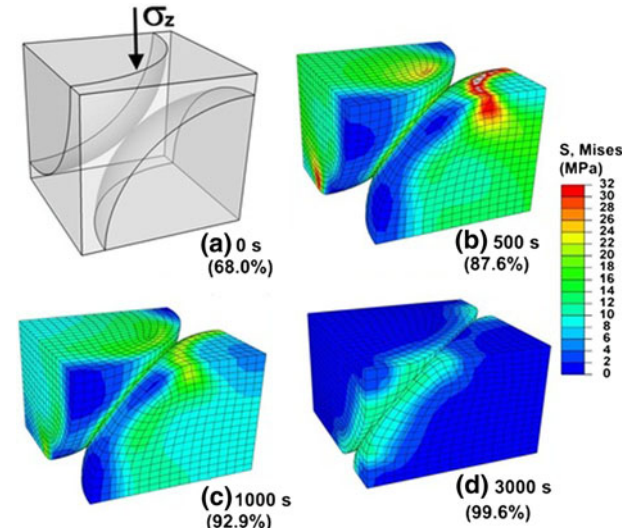


Fig. 4—FE densification simulation for bcc configuration: (a) initial powders with relative density 68 pct, and (b-d) von Mises stress contour plot of deformed powders at different time for Ti-6Al-4V at 15 MPa applied stress and 1293 K (1020 °C). The gray region represents stress greater than maximum stress in the color scale. The densification times and relative density are given under each figure.

The stress/strain-rate relation was provided as tabulated data based on the creep equation (Eq. [1]). Conceptually, because the yield stress is close to zero in the rate-dependent, perfectly-plastic material, at any applied stress, plastic strain develops continuously as long as the strain rate is within the range of validity of the creep equation (Eq. [1]) or equivalently the rate-dependent plasticity equation (Eq. [5]). However, if there is a slight increase in strain rate, the yield stress increases so that it is larger than the applied stress, *i.e.*, the material does not yield any more and the plastic deformation stops until the rate decreases so that the material is in a yield condition again. Also in Eq. [5], there is no work hardening component, and previous strain history has no influence on strain rate under a specific stress. In this manner, the creep equation is always satisfied. This approach to powder compaction simulation by rate-dependent plasticity increased the computational speed significantly and allowed the implementation of more complex material behavior including both creep and rate-dependent plastic deformation.

B. Simple Cubic Array of Powders

A simple cubic (sc) infinite array of spherical powders is simulated by 1/8 of a single spherical powder, using

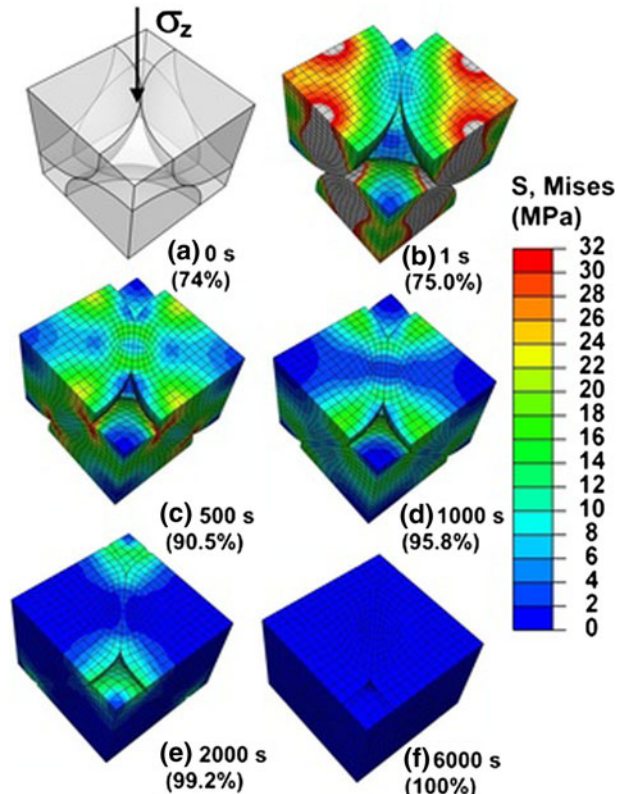


Fig. 5—FE densification simulation for fcc configuration: (a) initial powders with relative density 74 pct and (b–f) von Mises stress contour plot of deformed powders at different time for Ti-6Al-4V at 15 MPa applied stress and 1293 K (1020 °C). The gray region represents stress greater than maximum stress in the color scale. The densification times and relative density are given under each figure.

symmetry considerations with appropriate periodic boundary conditions. This was achieved by confining the powder in a virtual box, cubic in shape at the onset of the simulation, so that contact between powders was enforced. The box with two square pistons located at the top and bottom was modeled as a 3D discrete rigid object, and the powder was modeled as a 3D deformable object. Constant pressure was applied on the upper piston, which was allowed to translate in the z direction only, whereas the lower piston and the sides of the box were fixed so that the powder deformed along the z direction (Figure 1(a)) with no preferred deformation in the deformation taking place in the horizontal directions (x-y plane). Figure 1 shows von Mises stress contours in the powder deformed to three levels corresponding to 70 pct, 80 pct, and 99 pct relative densities (calculated as ratio of powder to box volume).

The creep- and rate-dependent plasticity approaches were implemented in the material properties module of ABAQUS. Densification curves calculated for creep under isothermal condition are shown in Figure 2(a): Negligible differences were found between these two implementations and the simulations with different mesh

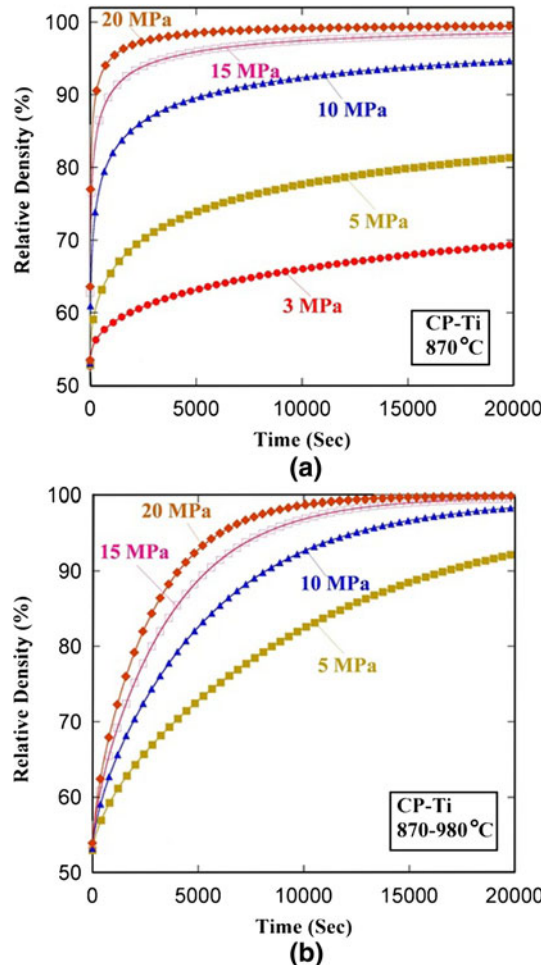


Fig. 6—FE densification curves (sc configuration) for CP-Ti powders at various stresses for (a) isothermal creep at 1143 K (870 °C) and (b) transformation mismatch plasticity during thermal cycling 1133 K to 1253 K (860 °C to 980 °C).

density under the rate-dependent plasticity approach converged. Similar results are achieved for densification curves for transformation-plasticity under thermal cycling conditions (Figure 2(b)). Given that there was no distinction between these two approaches, the densification simulations discussed in the following sections were based mostly on the rate-dependent plasticity approach (Eq. [5]) to increase computational speed.

C. Centered Cubic Arrays of Powders

Increased complexity is captured in a simple cubic configuration with two different powder sizes (sc-2) as well as in body-centered cubic (bcc) and fcc arrays of single-size powders, with symmetry allowing the use of two and four eighths of spheres, as illustrated in Figures 3 through 5. It is technically important to consider consolidation with mixed particle sizes (sc-2 in this study) and different shapes to capture finer features during consolidation (such as higher stress on smaller

powder) as recognized in the continuum modeling in the literature.^[44,45] In this study, to account for the different powder size for better initial relative density (60 pct), powders with two sizes (with a radius ratio of 1.566:1) and equal number were packed in simple cubic configuration (or alternating along all three directions) as shown in Figure 3. In contrast with the condition of no sliding among powders used in the single-powder sc configuration, interpowder sliding in the sc-2, and the bcc and fcc configurations is allowed to reflect the nature of multipowder deformation during densification. As a result, the number of intercontact regions increases, and so does the computational expense. Because ABAQUS has the capability to track self-contact with possible separation and sliding, the spherical powders were grouped or merged into one part in ABAQUS to use the self-contact function, although the grouped powders were not in contact in the initial state. In this manner, only the contacts and possible contacts (defined as intercontact in ABAQUS) between powders

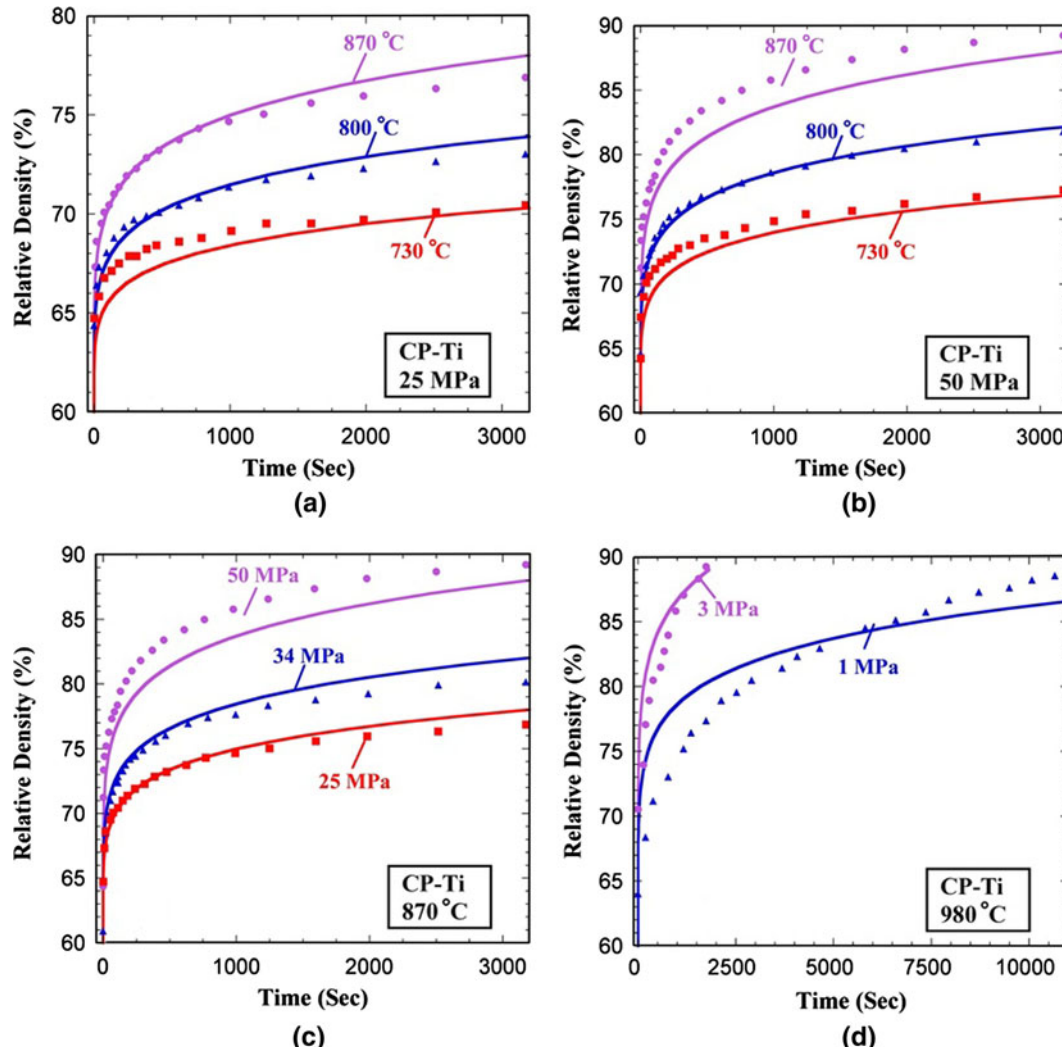


Fig. 7—Densification curves for CP-Ti showing experimental data (from Ref. 10 for α -Ti and from Ref. 15 for β -Ti), and current FE model predictions (sc configuration with stress knock-down factors f) for isothermal conditions (a) α -Ti at 25 MPa and 1003 K, 1073 K, and 1143 K (730 °C, 800 °C, and 870 °C) ($f = 0.17$), (b) α -Ti at 50 MPa and 1003 K, 1073 K, and 1143 K (730 °C, 800 °C, and 870 °C) ($f = 0.17$), (c) α -Ti at 1143 K (870 °C) and 25, 34, 50 MPa ($f = 0.17$), and (d) β -Ti at 1253 K (980 °C) and 1 MPa ($f = 1$) and 3 MPa ($f = 0.6$).

and the cubic box, and the base and top piston needed to be specified. Although the intercontact can be automatically searched and established by ABAQUS based on interseparation criteria, the intercontacts were specified individually because the number of intercontacts was still manageable even in the case of bcc and fcc configurations. During the compaction of monosized powders, all the powders deformed equally as shown in Figures 4 and 5. In contrast, for powders with bimodal size distribution, smaller powders are deformed more heavily than the larger powders, as shown in Figure 3 and as reported by Li and Funkenbusch.^[45,46]

III. RESULTS AND DISCUSSION

A. Densification of CP-Ti Powders

The effect of applied stress on densification of CP-Ti powders is shown for the sc configuration in Figure 6(a) for isothermal creep and in Figure 6(b) for transformation-plasticity caused by thermal cycling. As expected from the respective stress exponents, the effect of stress was more pronounced in the former case than in the latter. Another notable difference between the two cases is the densification behavior for long times ($>10,000$ seconds): Under creep conditions, a near horizontal plateau is reached (Figure 6(a)), whereas under superplastic conditions, the curve retains a positive slope indicating that full density is achievable in a shorter time (Figure 6(b)).

Two previous studies on CP-Ti powder hot pressing were carried out at temperatures where titanium is in its α -phase [1003 K, 1073 K, and 1143 K (730 °C, 800 °C, and 870 °C)]^[10,15] or its β -phase 1253 K (980 °C).^[10,15] The experimental densification curve measurements were compared with models based on dislocation creep mechanism (Eq. [2]). For isothermal conditions, CP-Ti followed a power-law creep (Eq. [1]) with creep stress exponent $n = 4.3$ and power law creep constant C . For the α -phase CP-Ti, C takes values of 1.29×10^{-10} , 7.72×10^{-10} , and $3.86 \times 10^{-9} \text{ MPa}^{-4.3} \text{s}^{-1}$ at 730, 1073 K, and 1143 K (800 °C and 870 °C), respectively.^[10,47] For β -phase CP-Ti at 1253 K (980 °C), C is $6.74 \times 10^{-6} \text{ MPa}^{-4.3} \text{s}^{-1}$.^[48] Modeling of powder densification with Eq. [2] assumed ideal condition without friction; however, the friction was high in these experiments^[10] because of the absence of lubricant coating between the CP-Ti preform and the molybdenum die wall. We introduce a “knock-down factor” f to account for the friction effect on the effective applied stress in Eqs. [2] and [3] by multiplying the effective stress with f . For α -Ti powder densification,^[10] a single knock-down factor $f = 0.17$ resulted in reasonable agreement between the measured and calculated densification curves for the three applied stresses (25, 34, and 50 MPa) and three temperatures [1003 K, 1073 K, and 1143 K (730 °C, 800 °C, and 870 °C)], as shown in Figures 7(a) through (c). Calculated and measured densification curves for β -Ti at 1253 K (980 °C) are shown in Figure 7(d). To achieve reasonable agreement with the experimental curves,^[15] the knock-down factors

for the applied stresses of 1 and 3 MPa are unity (indicating no friction) and 0.6, respectively. The reduced level of correction caused by friction (knock-down factor closer to unity) may be due to the result of much lower applied stresses (1–3 vs 25–50 MPa) and the larger die area (10.4 vs 1.2 cm²).

B. Densification of Ti-6Al-4V Powders

The densification curves calculated for Ti-6Al-4V powders are shown for isothermal conditions [1293 K (1020 °C)] in Figure 8(a) and for thermal cycling conditions [1133 K to 1293 K (860 °C to 1020 °C)] in Figure 8(b) for the sc configuration. The same trends found for CP-Ti (Figures 6(a) and (b)) are apparent, illustrating that transformation mismatch plasticity, despite the lower average temperature, significantly enhances densification rates for low applied stress (e.g., 5 MPa) and when relative density is high, i.e., when interparticle stresses are relatively low.

Figures 9(a) through (d) show, for isothermal densification under applied stresses of 5, 10, 15, and 20 MPa, a comparison between FE modeling, continuum mod-

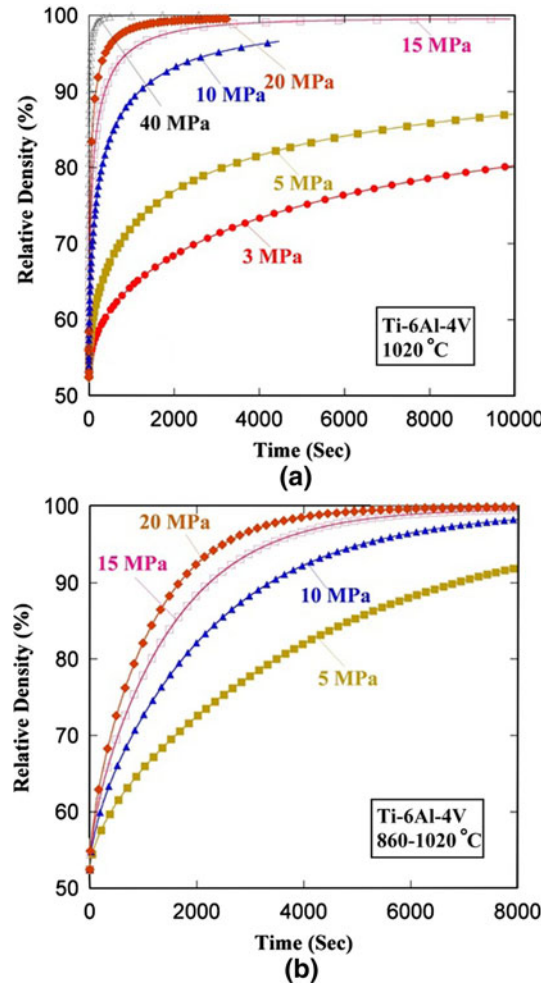


Fig. 8—Stress effect on Ti-6Al-4V densification simulation of single powder in sc configuration based on (a) creep and (b) transformation mismatch plasticity.

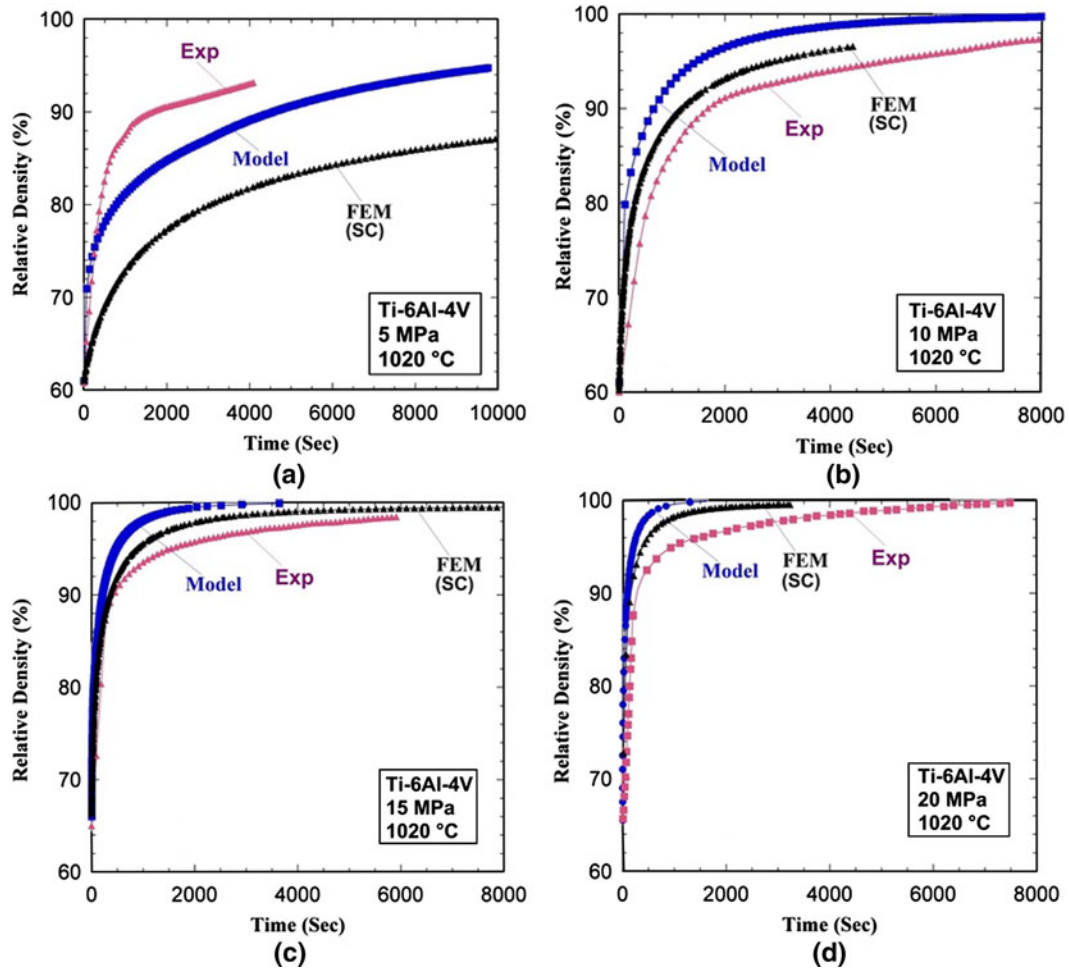


Fig. 9—Densification curves for Ti-6Al-4V showing experimental data (Exp label) and continuum model (Model) predictions (both from Ref. 16), and current FE mode (FE) predictions (sc configuration with no stress knock-down factors) for isothermal conditions at 1293 K (1020 °C) for applied stresses of (a) 5 MPa, (b) 10 MPa, (c) 15 MPa, and (d) 20 MPa.

eling, and experiments for rounded plasma rotating electrode process (PREP) powders.^[16] Reasons for the discrepancy between the continuum model and the FE calculations include the different particle packing and the transition from initial to final stage. A discrepancy with experimental data may be caused by friction effects, as discussed previously (no knock-down factor was used in Figures 9(a) through (d)). A similar comparison is given, for applied stresses of 5, 10, and 15 MPa, in Figures 10(a) through (c) for the case of densification under thermal cycling conditions when transformation-mismatch plasticity is active. The agreement is, in most cases, adequate among the continuum model, the experimental measurements, and the FE simulation with various powder configurations (and no knock-down factor). The sc configuration with two different powder sizes, with an initial relative density close to 60 pct, gives the best match with the experimental measurement (Figure 10) for hydrogenation/dehydrogenation (HDH) and PREP powders. Another observation is that the sc configuration takes longer to reach a given density compared with the bcc and fcc configurations, in part because of the lower initial density.

However, in the case of dislocation creep densification under isothermal condition, sc packing (Figures 9(a) through (d)) has a better agreement with experimental data; under thermal cycling conditions (Figures 10(a) through (c)), bcc and fcc configurations give a better match. Initial bcc and fcc configurations are closer to the configuration assumed in the continuum model (powder coordination number of 7.7) with initial relative density close to the bcc configuration (powder coordination number of 8). As expected, the FE results with sliding are in better agreement with the continuum models for these more realistic powder packings (two-powder sc, bcc, and fcc) and in reasonable agreement with experimental measurements, given the simplifications used in the model. The difference in densification kinetics between bcc and fcc is small, and it may be caused by different initial density and different slipping contributions. More complex models capturing particle size distribution, random particle packing, and more accurate powder sliding will be needed to improve agreement with experiments.

The effect of powder shape is illustrated in Figure 11, which shows FE densification curves (for the sc

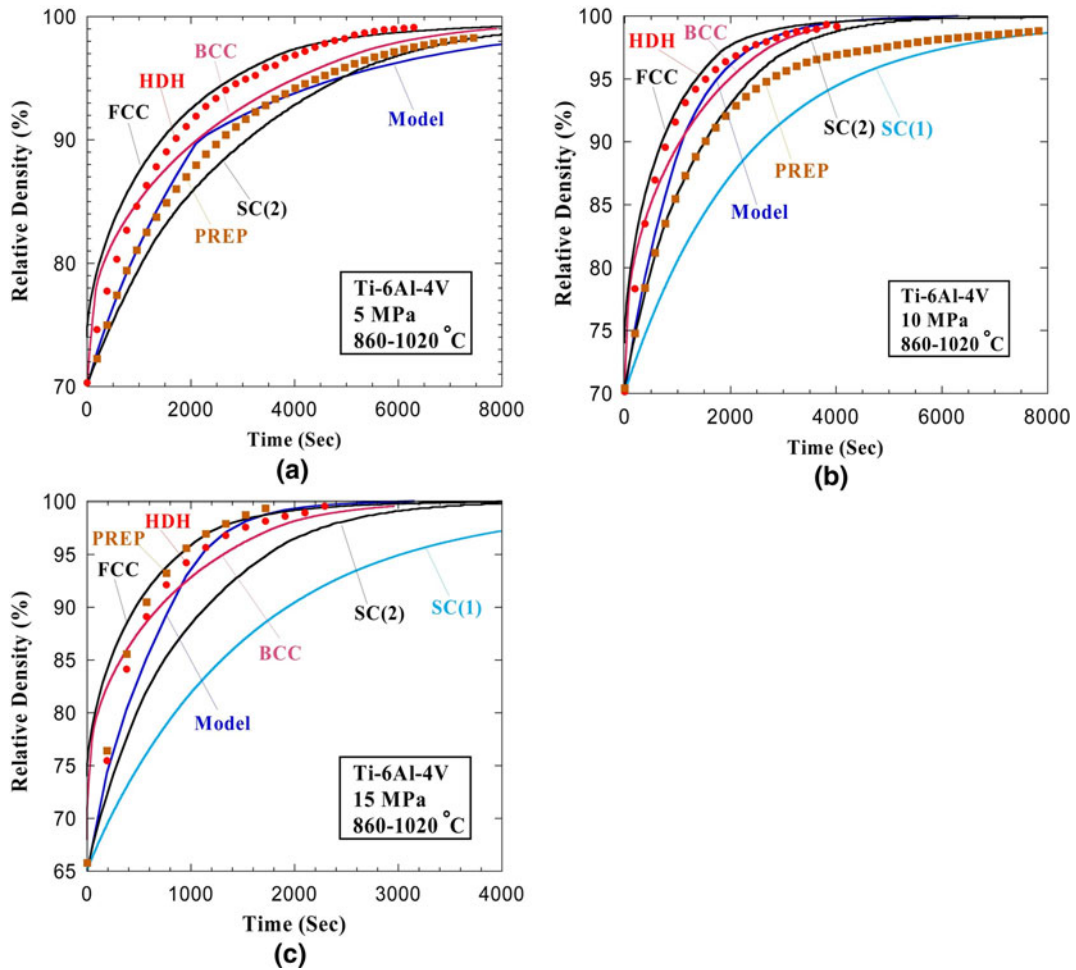


Fig. 10—Densification curves for Ti-6Al-4V showing experimental data (HDH and PREP) and continuum model (Model) predictions (both from Reference 16) and current FE model predictions (sc, sc(2), fcc, and bcc configurations with no stress knock-down factors) for thermal cycling conditions [1133 K to 1293 K (860 °C to 1020 °C)] and applied stresses of (a) 5 MPa, (b) 10 MPa, and (c) 15 MPa.

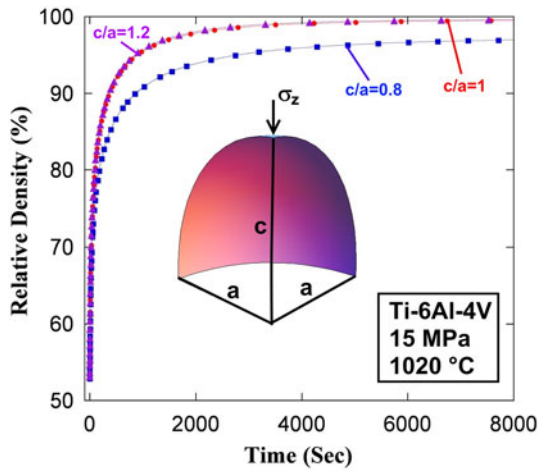
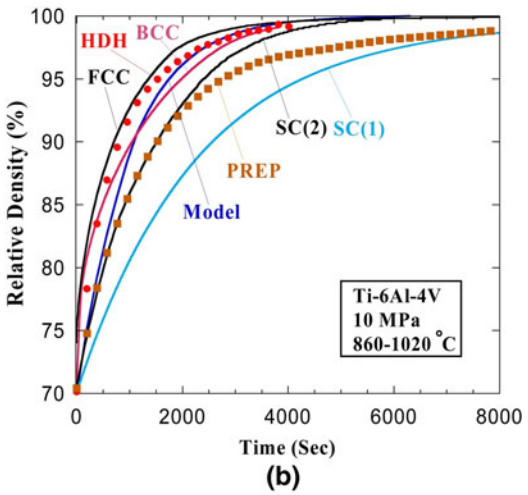


Fig. 11—FE densification curves for sc configuration of Ti-6Al-4V powders at 1293 K (1020 °C) for different aspect ratios of powders with applied stress of 15 MPa (loading direction is along c axis) with aspect ratio $c/a = 1.2$, 1, and $1/1.2 = 0.8$.

configuration under isothermal conditions and 15 MPa) for powders with the following aspect ratio c/a (where a and c are the powder axes perpendicular and parallel to



the applied stress, respectively): $c/a = 1.2$ (prolate spheroids), $c/a = 1$ (spheres), and $c/a = 1/1.2 = 0.8$ (oblate spheroids). The densification kinetics are nearly identical for $c/a = 1.2$ and 1 but clearly slower for $c/a = 0.8$. A likely reason is that the latter configuration requires the largest powder strain (which is predominantly uniaxial compressive, in the direction of the applied stress) to fill the gap between the powders for full densification.

Double-logarithmic plots of densification rate vs relative density are shown in Figure 12(a) for various applied stresses. The rates were calculated by taking every five density points in the FE simulations for sc configuration under isothermal condition. It is apparent that these plots are linear over most of the density range, i.e., from ~60 pct to ~90 pct (the onset of final stage densification), with the same slope for the various applied stresses between 5 and 40 MPa, where the initial stage densification (up to 90 pct relative density) is relatively short. According to the continuum model (Eqs. [4] and [5]), at a specific relative density, the densification rate is proportional to σ^n , the applied stress raised to the power exponent n . Then, normalizing the densification rate by σ^n should produce a unified master

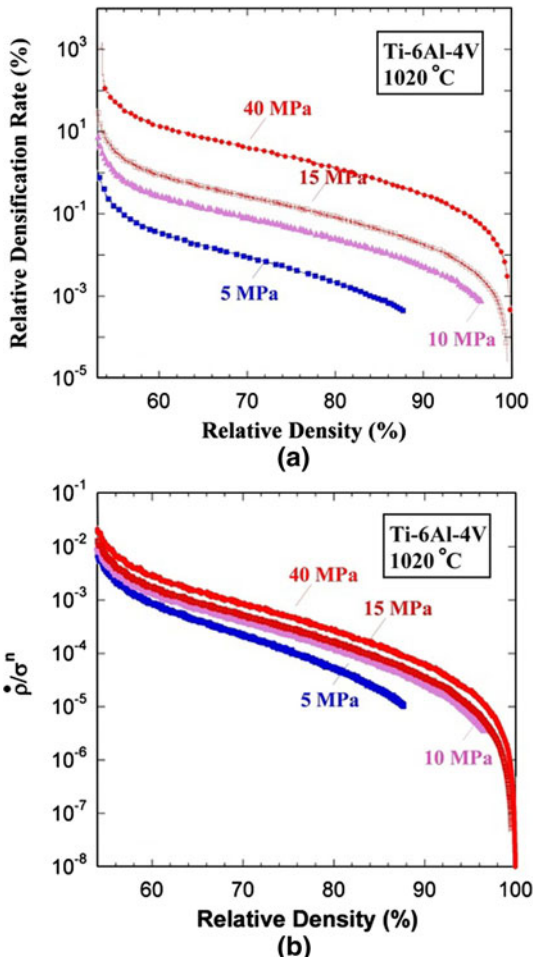


Fig. 12—(a) Double logarithmic plot of relative densification rate (FE calculations) vs relative density for Ti-6Al-4V at 1293 K (1020 °C) for various applied stresses; (b) same plot as in (a), but with densification rate normalized by applied stress raised to the power $n = 2.8$.

curve for all applied stresses. Using the FE data presented in Figure 12(a), this prediction from the continuum model is tested in Figure 12(b). The curves converge for applied stress values spanning 5–40 MPa, indicating a good match between continuum and numerical models, and indicating that the simple continuum model for densification is a good approximation and that only small improvements in predicted densification kinetics can be expected from the much more complex and time-consuming FE model. This model, however, provides interesting insights on the stress distribution within the powders, which is an effect of initial packing and powder shape.

IV. CONCLUSIONS

FE modeling was conducted to describe CP-Ti or Ti-6Al-4V powder densification for uniaxial die pressing at an increased temperature under isothermal conditions (where power-law creep controls powder deformation)

or under thermal cycling conditions (where transformation-mismatch plasticity is controlling). The following main conclusions are reached:

1. For isothermal densification in the α - or β -fields of CP-Ti, reasonable agreement is found between the FE models and experimental measurement in the literature.
2. For isothermal densification at 1293 K (1020 °C) of β -Ti-6Al-4V, predictions from FE simulation and continuum modeling are in general agreement with literature experimental densification measurement under different applied stress.
3. For thermal cycling densification of Ti-6Al-4V via transformation superplasticity over the α - β -field, FE simulations with bcc and fcc powder configurations show a better match than sc configuration compared with the literature experimental measurement.
4. The good agreement between the complex FE model and the simpler continuum model indicates that for both thermal cycling and isothermal conditions, the latter model can be used with reasonable accuracy.

ACKNOWLEDGMENTS

This research was supported by a grant from the Boeing Corporation. The authors thank Mr. L.C. Firth (The Boeing Company) for useful discussions. This article is dedicated to the memory of Dr. W.B. Crow (The Boeing Company) who made numerous important contributions to the current research.

REFERENCES

1. R.R. Boyer: *Mater. Sci. Eng. A*, 1996, vol. 213, pp. 103–14.
2. M. Peters, J. Kumpfert, C.H. Ward, and C. Leyens: *Adv. Eng. Mater.*, 2003, vol. 5, pp. 419–27.
3. M. Niinomi: *Mater. Sci. Eng. A*, 1998, vol. 243, pp. 231–36.
4. M. Geetha, A.K. Singh, R. Asokamani, and A.K. Gogia: *Progr. Mater. Sci.*, 2009, vol. 54, pp. 397–425.
5. K. Wang: *Mater. Sci. Eng. A*, 1996, vol. 213, pp. 134–37.
6. H.J. Rack and J.I. Qazi: *Mater. Sci. Eng. C*, 2006, vol. 26, pp. 1269–77.
7. D.S. Wilkinson and M.F. Ashby: *Acta Metall.*, 1975, vol. 23, pp. 1277–85.
8. E. Arzt, M. Ashby, and K. Easterling: *Metall. Trans. A*, 1983, vol. 14A, pp. 211–21.
9. A.S. Helle, K.E. Easterling, and M.F. Ashby: *Acta Metall.*, 1985, vol. 33, pp. 2163–74.
10. N. Taylor, D.C. Dunand, and A. Mortensen: *Acta Metall. Mater.*, 1993, vol. 41, pp. 955–65.
11. C. Schuh and D.C. Dunand: *Acta Mater.*, 2001, vol. 49, pp. 199–210.
12. Q. Li, E. Chen, D. Bice, and D. Dunand: *Metall. Mater. Trans. A*, 2007, vol. 38A, pp. 44–53.
13. Y.-M. Liu, H.N.G. Wadley, and J.M. Duva: *Acta Metall. Mater.*, 1994, vol. 42, pp. 2247–60.
14. J.M. Duva and P.D. Crow: *Acta Metall. Mater.*, 1992, vol. 40, pp. 31–35.
15. C. Schuh, P. Noel, and D.C. Dunand: *Acta Mater.*, 2000, vol. 48, pp. 1639–53.
16. B. Ye, M.R. Matsen, and D.C. Dunand: *Acta Mater.*, 2010, vol. 58, pp. 3851–9.
17. G.W. Greenwood and R.H. Johnson: *Proc. Roy. Soc. Lond. Series A, Math. Phys. Sci.*, 1965, vol. 283, pp. 403–22.

18. P. Zwigl and D. Dunand: *Metall. Mater. Trans. A*, 1998, vol. 29A, pp. 2571–82.
19. C. Schuh and D.C. Dunand: *J. Mater. Res.*, 2001, vol. 16, pp. 865–75.
20. D.C. Dunand and S. Myojin: *Mater. Sci. Eng. A*, 1997, vol. 230, pp. 25–32.
21. M. Abouaf, J.L. Chenot, G. Raïsson, and P. Bauduin: *Int. J. Numer. Meth. Eng.*, 1988, vol. 25, pp. 191–212.
22. N.A. Fleck, L.T. Kuhn, and R.M. McMeeking: *J. Mech. Phys. Solid.*, 1992, vol. 40, pp. 1139–62.
23. P. Sofronis and R.M. McMeeking: *J. Appl. Mech.*, 1992, vol. 59, pp. S88–S95.
24. L.T. Kuhn and R.M. McMeeking: *Int. J. Mech. Sci.*, 1992, vol. 34, pp. 563–73.
25. K.T. Kim and J.H. Cho: *Int. J. Mech. Sci.*, 2001, vol. 43, pp. 2929–46.
26. H. Li, S. Saigal, and P.T. Wang: *Acta Mater.*, 1996, vol. 44, pp. 2591–98.
27. I. Sridhar, N.A. Fleck, and A.R. Akisanya: *Int. J. Mech. Sci.*, 2001, vol. 43, pp. 715–42.
28. R. Gampala, D.M. Elzey, and H.N.G. Wadley: *Acta Mater.*, 1996, vol. 44, pp. 1479–95.
29. A.C.F. Cocks and I.C. Sinka: *Mech. Mater.*, 2007, vol. 39, pp. 392–403.
30. J. Xu and R.M. McMeeking: *Int. J. Mech. Sci.*, 1995, vol. 37, pp. 883–97.
31. P.A. Cundall and O.D.L. Strack: *Geotechnique*, 1979, vol. 29, pp. 47–65.
32. P. Redanz and N. Fleck: *IUTAM Symp. on Theoretical and Numerical Methods in Continuum Mechanics of Porous Materials*, 2002, pp. 293–98.
33. A.T. Procopio and A. Zavalaniogos: *J. Mech. Phys. Solid*, 2005, vol. 53, pp. 1523–51.
34. J. Zhang: *Compos. Sci. Technol.*, 2009, vol. 69, pp. 2048–53.
35. B. Harthong, J.F. Jerier, P. Doremus, D. Imbault, and F.V. Donze: *Int. J. Solid. Struct.*, 2009, vol. 46, pp. 3357–64.
36. J.F. Jerier, B. Harthong, D. Imbault, F.V. Donze, and P. Doremus: *Powders and Grains 2009: Proc. 6th Int. Conf. on Micromechanics of Granular Media*, 2009, vol. 1145, pp. 457–60.
37. J.E. Andrade and X. Tu: *Mech. Mater.*, 2009, vol. 41, pp. 652–69.
38. W.L. Roland, T.G. David, S.Y. Xinshe, and C.R. Ray: *Int. J. Numer. Meth. Eng.*, 2005, vol. 62, pp. 853–69.
39. D.T. Gethin, X.S. Yang, and R.W. Lewis: *Comput. Meth. Appl. Mech. Eng.*, 2006, vol. 195, pp. 5552–65.
40. G. Frening: *Comput. Meth. Appl. Mech. Eng.*, 2008, vol. 197, pp. 4266–72.
41. J.L. Choi and D.T. Gethin: *Model. Simulat. Mater. Sci. Eng.*, 2009, vol. 17, p. 035005.
42. A. Munjiza and K.R.F. Andrews: *Int. J. Numer. Meth. Eng.*, 1998, vol. 43, pp. 131–49.
43. X. Ma and D.Z. Zhang: *J. Mech. Phys. Solid.*, 2006, vol. 54, pp. 1426–48.
44. S. Nair and J. Tien: *Metall. Trans. A*, 1987, vol. 18, pp. 97–107.
45. E.K.H. Li and P.D. Funkenbusch: *Acta Metall.*, 1989, vol. 37 (6), pp. 1645–55.
46. E.K.H. Li and P.D. Funkenbusch: *Metall. Trans. A*, 1993, vol. 24, pp. 1345–54.
47. H.J. Frost and M.F. Ashby: *Deformation-Mechanism Maps: The Plasticity and Creep of Metals and Ceramics*, 1st ed., Pergamon Press, New York, 1982, p. 184.
48. C. Schuh and D.C. Dunand: *Scripta Mater.*, 2001, vol. 45, pp. 1415–21.